Applied Physics Letters

Six dimensional X-ray Tensor Tomography with a compact laboratory setup

Cite as: Appl. Phys. Lett. **109**, 134102 (2016); https://doi.org/10.1063/1.4963649
Submitted: 05 August 2016 . Accepted: 09 September 2016 . Published Online: 26 September 2016

Y. Sharma, M. Wieczorek, F. Schaff, S. Seyyedi, F. Prade, F. Pfeiffer, and T. Lasser

View Online Export Citation CrossMark

ARTICLES YOU MAY BE INTERESTED IN

Dual phase grating interferometer for tunable dark-field sensitivity
Applied Physics Letters **110**, 014105 (2017); https://doi.org/10.1063/1.4973520

Large field-of-view tiled grating structures for X-ray phase-contrast imaging
Review of Scientific Instruments **88**, 015104 (2017); https://doi.org/10.1063/1.4973632

Trochoidal X-ray Vector Radiography: Directional dark-field without grating stepping
Applied Physics Letters **112**, 111902 (2018); https://doi.org/10.1063/1.5020361

© 2016 Author(s).

Six dimensional X-ray Tensor Tomography with a compact laboratory setup

Y. Sharma,[1,2] M. Wieczorek,[2] F. Schaff,[1] S. Seyyedi,[2,1] F. Prade,[1] F. Pfeiffer,[1,3] and T. Lasser[2]

[1]*Lehrstuhl für Biomedizinische Physik, Physik-Department and Institut für Medizintechnik, Technische Universität München, 85748 Garching, Germany*
[2]*Computer Aided Medical Procedures, Technische Universität München, 85748 Garching, Germany*
[3]*Institut für diagnostische und interventionelle Radiologie, Klinikum rechts der Isar, Technische Universität München, 81675 München, Germany*

(Received 5 August 2016; accepted 9 September 2016; published online 26 September 2016)

Attenuation based X-ray micro computed tomography (XCT) provides three-dimensional images with micrometer resolution. However, there is a trade-off between the smallest size of the structures that can be resolved and the measurable sample size. In this letter, we present an imaging method using a compact laboratory setup that reveals information about micrometer-sized structures within samples that are several orders of magnitudes larger. We combine the anisotropic dark-field signal obtained in a grating interferometer and advanced tomographic reconstruction methods to reconstruct a six dimensional scattering tensor at every spatial location in three dimensions. The scattering tensor, thus obtained, encodes information about the orientation of micron-sized structures such as fibres in composite materials or dentinal tubules in human teeth. The sparse acquisition schemes presented in this letter enable the measurement of the full scattering tensor at every spatial location and can be easily incorporated in a practical, commercially feasible laboratory setup using conventional X-ray tubes, thus allowing for widespread industrial applications.
© 2016 Author(s). All article content, except where otherwise noted, is licensed under a Creative Commons Attribution (CC BY) license (http://creativecommons.org/licenses/by/4.0/).
[http://dx.doi.org/10.1063/1.4963649]

Conventional X-ray imaging is based on the attenuation of X-rays when they pass through a material. Recently, grating interferometer based approaches[1–3] are being used to exploit the scattering and refraction of X-rays by the material in order to obtain additional contrast modalities, namely, phase contrast and dark-field contrast. Dark-field contrast originates from the ultra-small angle scattering of X-rays by sub-micron and micron sized structures.[4–8] Unlike attenuation, the dark-field signal obtained in a grating interferometer is anisotropic in nature,[9–11] which means that the measured signal depends on the orientation of the scattering structure with respect to the grating interferometer. Thus, by varying the relative orientation of a scattering structure within the interferometer, it is possible to deduce information about its orientation from the variations in the dark-field signal.

Two dimensional structure orientations can be recovered from several projections acquired by rotating the sample around the beam propagation direction.[12,13] However, in order to measure the structure orientations in three dimensions, Malecki *et al.*[14] introduced several non-standard acquisition poses in a technique called X-ray Tensor Tomography (XTT). This was achieved by placing the sample on an Eulerian cradle (Figure 1), which allows rotation of the sample with three degrees of freedom, and not just around one axis as done in conventional tomography. The three degrees of freedom are achieved by rotating the cradle around the y axis (angle ψ), rotating the sample stage around the z' axis by moving it on the cradle (angle θ), and rotating the sample around the y' axis (angle ϕ); here, the coordinate system (x, y, z) denotes world coordinates, and (x', y', z') is the sample coordinate frame (Figure 1). A standard XTT dense sampling scheme S comprises several acquisition poses s_i

$$S = \{s_i := (\psi, \theta, \phi); \quad \psi \in \{0°, 20°, 40°\}, \theta \in \Theta, \phi \in \Phi\},$$

where $\Theta = \{0°, 30°, 60°, 90°\}$, $\Phi = \{0°, 2.01°, \ldots, 360°\}$. Such an acquisition geometry enables the measurement of the anisotropic dark-field signal from several poses spread over the unit sphere. These dark-field projections are then fed into an iterative reconstruction algorithm,[15] which splits the combined signal measured in all the projections into several auxiliary scattering components, each of which determines the strength of scattering along a unique orientation. The scattering orientations are then scaled with their respective scattering strengths, and a Principal Component Analysis is performed to fit a scattering tensor in each voxel. At last, the structure orientation is approximated as the smallest half axis of the

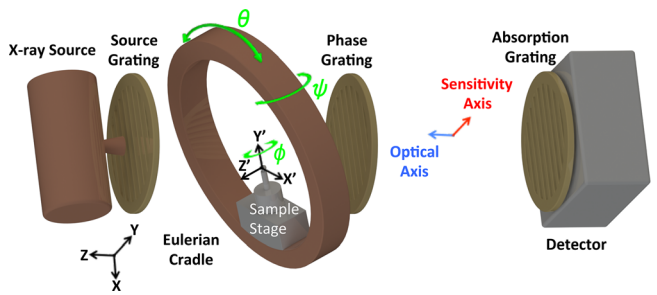

FIG. 1. Schematic of the X-ray Tensor Tomography grating interferometer setup showing a non-standard acquisition pose and the three axes of rotation.

 © Author(s) 2016.

tensor. An illustration of the XTT acquisition and reconstruction method is shown in Figure 2.

XTT is a promising technique with a number of applications such as visualization of the microstructure of fibrous materials and dentinal tubules of human teeth.[14,15] It is, however, limited by long acquisition times owing to the large number of measurements and the time required for the movement of several motors. Moreover, the Eulerian cradle is a bulky component and poses challenges for a compact setup design. Hence, there is a need to optimize the XTT acquisition geometry. In order to do so, it is essential to establish a relationship between the acquisition geometry and the expected result.

In order to visualize the acquisition geometries, we formulate an example tomographic trajectory rotating about y' as a function of ψ and θ

$$A(\psi,\theta) := \{x := (\psi,\theta,\phi); \quad \phi \in [0^\circ, 18.95^\circ, \ldots, 360^\circ]\}.$$

A common sparse acquisition scheme for conventional computed tomography (CT) using 20 equally spaced projection angles is then expressed as $A(0^\circ, 0^\circ)$. In other words, the sample is rotated around the fixed y axis and line integrals through the sample along z, also known as the optical axis, are recorded. Let us define $\hat{t}(x)$ as the unit vector along the optical axis for a given acquisition pose $x := (\psi,\theta,\phi)$. For visualization, we plot $\pm\hat{t}(x)$ on a unit sphere, assuming that the sample is fixed at the center of the sphere. The points $\pm\hat{t}(x)$ for $A(0^\circ, 0^\circ)$ are shown in blue in Figure 3(a). Another important variable for XTT is the normalized sensitivity axis $\hat{s}(x)$. The sensitivity axis of a grating interferometer is the direction in which the phase shift of X-rays is measured. It lies in the plane of the gratings, orthogonal to the grating bars (Figure 1). We have $\hat{s}(x) = y$ when the grating bars are horizontal. Assuming again that the sample is fixed at the center of a sphere, we also plot $\pm\hat{s}(x)$ on the unit sphere. The points $\pm\hat{s}(x)$ for $A(0^\circ, 0^\circ)$ are shown in red in Figure 3(a). It can be seen that only one direction of scattering can be measured with $A(0^\circ, 0^\circ)$. Therefore, additional tomographic trajectories for XTT (as shown in Figure 3) are obtained by rotating y' using ψ and θ.

The visualization of the trajectories of the optical axis $\hat{t}(x)$ and sensitivity axis $\hat{s}(x)$ shown in Figure 3 gives a qualitative understanding of the orientations that are measured with a given acquisition scheme. Below, we present a method for the quantification of such acquisition schemes.

Let Σ and $\mathcal{T}$ be the two sets of evenly distributed points chosen from a hemisphere

$$\Sigma = \{\sigma_k,\ k = 1, 2, \ldots, N\},$$
$$\mathcal{T} = \{\tau_j,\ j = 1, 2, \ldots, N\},$$

where $N = 4843$. The mean vector of Σ is given by

$$m_\Sigma = \frac{1}{N}\sum_{k=1}^{N}\sigma_k.$$

Let X be an acquisition scheme using n different acquisition poses x_i

$$X := \{x_i := (\psi_i, \theta_i, \phi_i); \quad i = 1, \ldots, n\}.$$

The objective is to define a quantity, *Coverage*(X, k), that represents how well the orientation $\sigma_k \in \Sigma$ is measured by X. Our proposed procedure for computing *Coverage*(X, k) is outlined in the following:

(1) Define $X_k \subset X$ as the set of poses that measure the orientation $\sigma_k \in \Sigma$

$$X_k := \{x \in X; \quad w(\sigma_k, x) > T_c\},$$

where $w(\sigma_k, x)$ is a weight factor that specifies how well the orientation σ_k is measured by the acquisition pose x, and $T_c = 0.7$ is an arbitrarily chosen threshold. $w(\sigma_k, x)$ is given by

$$w(\sigma_k, x) = \left(|\sigma_k \times \hat{t}(x)|\ \langle \sigma_k, \hat{s}(x)\rangle\right)^2, \tag{1}$$

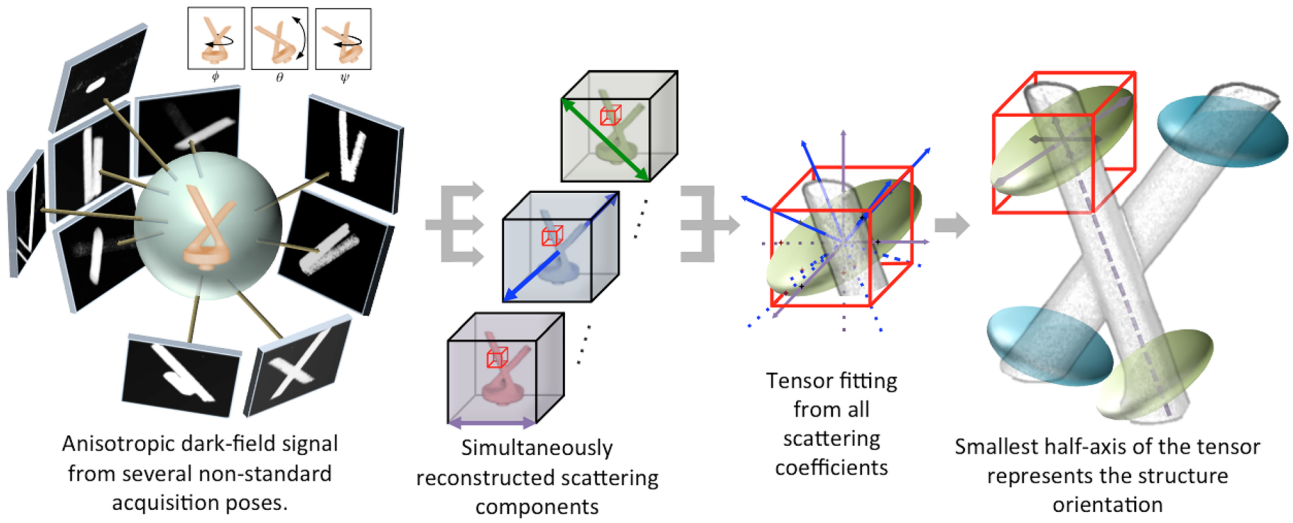

FIG. 2. Demonstration of the X-ray Tensor Tomography acquisition and reconstruction method for a phantom consisting of only two main orientations. Several dark-field projections of the sample are acquired over the unit sphere, unlike XCT where projections are acquired only on a circular trajectory. The combined signal acquired in all the projections is reconstructed into several volumes, each representing the strength of scattering along a unique orientation. The scattering strengths along all orientations are used to fit a tensor for every voxel. The smallest half axis of the tensor represents the structure orientation.

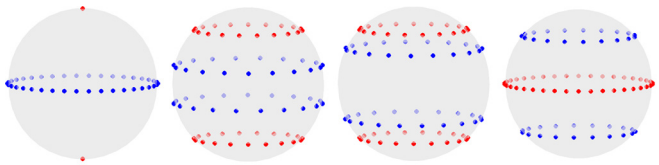

(a) $A(0°, 0°)$ (b) $A(20°, 45°)$ (c) $A(40°, 45°)$ (d) $A(40°, 90°)$

FIG. 3. Spherical representation of acquisition scheme $A(\psi, \theta)$ for different combinations of ψ and θ. On each sphere, blue points represent the trajectories of the optical axis $\pm\hat{t}(x)$, and red points represent the trajectories of the sensitivity axis $\pm\hat{s}(x)$ assuming that the sample is fixed at the center of the sphere.

where $|\cdot \times \cdot|$ denotes the magnitude of the cross product and $\langle\cdot,\cdot\rangle$ denotes the standard scalar product.

(2) R_k is the mean resulting length of the vectors $\hat{t}(x)$ for all $x \in X_k$

$$R_k = \left\| \frac{1}{|X_k|} \sum_{x \in X_k} \hat{t}(x) \right\|,$$

where $\|\cdot\|$ denotes the Euclidean length of a vector.

(3) $\mathcal{T}_k \subset \mathcal{T}$ is the set of points that are measured by X_k, assuming that each vector $\hat{t}(x)$ contributes to the measurement of points lying within a cone of opening angle 5° around it

$$\mathcal{T}_k := \{\tau \in \mathcal{T}; \quad \langle \tau, \hat{t}(x)\rangle > \cos(2.5°)\, \forall x \in X_k\}.$$

(4) The *Coverage*(X, k) is then defined as

$$Coverage(X,k) := 2 \times (1 - R_k) \times \frac{|\mathcal{T}_k|}{N}.$$

The quantity $2 \times (1 - R_k)$ is the spherical variance,[16] while $|\mathcal{T}_k|/N$ is related to the cumulative solid angle spanned by the $\hat{t}(x)$, $x \in X_k$. Thus, a higher value of *Coverage*(X, k) is achieved when the $\hat{t}(x)$ is distributed widely over the unit sphere.

Next, we scale the unit vectors $\sigma_k \in \Sigma$ with the values of *Coverage*(X, k) for all values of k resulting in

$$\Gamma(X) := \{\gamma_k := \sigma_k \times Coverage(X,k),\ k = 1, \ldots, N\},$$

and its mean

$$m_{\Gamma(X)} = \frac{1}{N} \sum_{k=1}^{N} \gamma_k.$$

The angular deviation of the normalized mean vector $\hat{m}_{\Gamma(X)}$ from the normalized mean vector $\hat{m}_\Sigma$ is a measure of the non-uniformity of the Coverage Sphere. Finally, we can now introduce the proposed Coverage Metric *CM*(X) as

$$CM(X) := \langle \hat{m}_{\Gamma(X)}, \hat{m}_\Sigma \rangle \times \frac{1}{N} \sum_{k=1}^{N} Coverage(X,k).$$

$CM(X) \in [0, 1]$ is a measure of the efficiency of the acquisition protocol X. Higher values of *CM* imply a more comprehensive and uniform measurement of all orientations on the unit sphere.

In order to correlate the concept of coverage with experimental observations and to study the effect of sparse acquisition schemes, a Short Fiber Reinforced Polymer (SFRP) sample made of glass fibers (18 μm in diameter) is analyzed. SFRPs are widely used in the automotive industry for their improved mechanical properties, which depend heavily on the orientation and length distribution of the reinforcing carbon or glass fibers. A very high resolution X-ray micro computed tomography (XCT) technique combined with fiber tracking techniques is commonly used to analyze the fiber orientation distribution of such materials.[17] XTT is a very useful technique for these materials as it directly resolves the orientations of the fibers within a much larger sample size. We measure a SFRP sample (dimensions $10 \times 10 \times 2$ mm) with the scheme S employing 3 axes of rotation, 7 phase steps, and 3 s exposure per phase step resulting in a total acquisition time of approximately 12.6 h. The setup[7] used for the XTT measurement comprises of a micro-focus X-ray tube (operated at voltage 45 kVp and power 25 W) and a Varian PaxScan 2520DX detector (pixel size 127 μm). The three gratings with periods of 10 μm, 5 μm, and 10 μm, respectively, were arranged in the first fractional Talbot configuration.

Scattering tensors $T_S(r_i) \in \mathbb{R}_+^{3\times3}$ for voxels r_i, $i = 1,\ldots, I$, discretizing the volume of interest (isotropic voxel size 64 μm^3), are calculated using the method proposed by Vogel *et al.*[15] and demonstrated in Figure 2; the subscript (here S) indicates the acquisition protocol used to compute the scattering tensors. Figure 4(a) shows the scattering tensors $T_S(r_i)$ along with the corresponding structure orientation overlaid on the XCT volume of the sample described above. The tensors are color coded with their orientation. It is evident from Figure 4(a) that XTT reveals the three dimensional orientations of the fibers in this sample. The resulting fiber orientations are comparable qualitatively to the fiber tracking results presented by Hannesschläger *et al.*[18] using a voxel size of 6.5 μm^3.

In the following, we will study sparse sampling schemes for XTT. S represents a densely sampled standard scheme within the practical limits of the hardware ($|\psi| > 40°$ is not achievable since the cradle would block the X-ray beam). XTT reconstructions of the SFRP sample are obtained using different acquisition schemes X and the resulting tensors $T_X(r_i)$ are compared to the base $T_S(r_i)$. For comparison, we compute a distance metric between corresponding tensors in each voxel. We use the Riemannian manifold Sym_3^+, i.e., the manifold of positive-definite symmetric matrices, equipped with a Riemannian metric.[20] The distance $d : \mathrm{Sym}_3^+ \times \mathrm{Sym}_3^+ \to \mathbb{R}_+$ between two tensors $T_1, T_2 \in \mathrm{Sym}_3^+$ on this manifold is then computed as

$$d(T_1, T_2) = \sqrt{\sum_{i=1}^{3} \log(\sigma_i)^2},$$

where σ_i denotes the i-th eigenvalue of the matrix $T_1^{-\frac{1}{2}} T_2 T_1^{-\frac{1}{2}}$. Two corresponding tensors $T_X(r_i)$ and $T_S(r_i)$ are considered to be correlated if $d(T_X(r_i), T_S(r_i))$ is less than a certain threshold T_p. Based on this, we introduce a Performance Metric *PM*(X), which determines how well the acquisition scheme X performs with respect to S

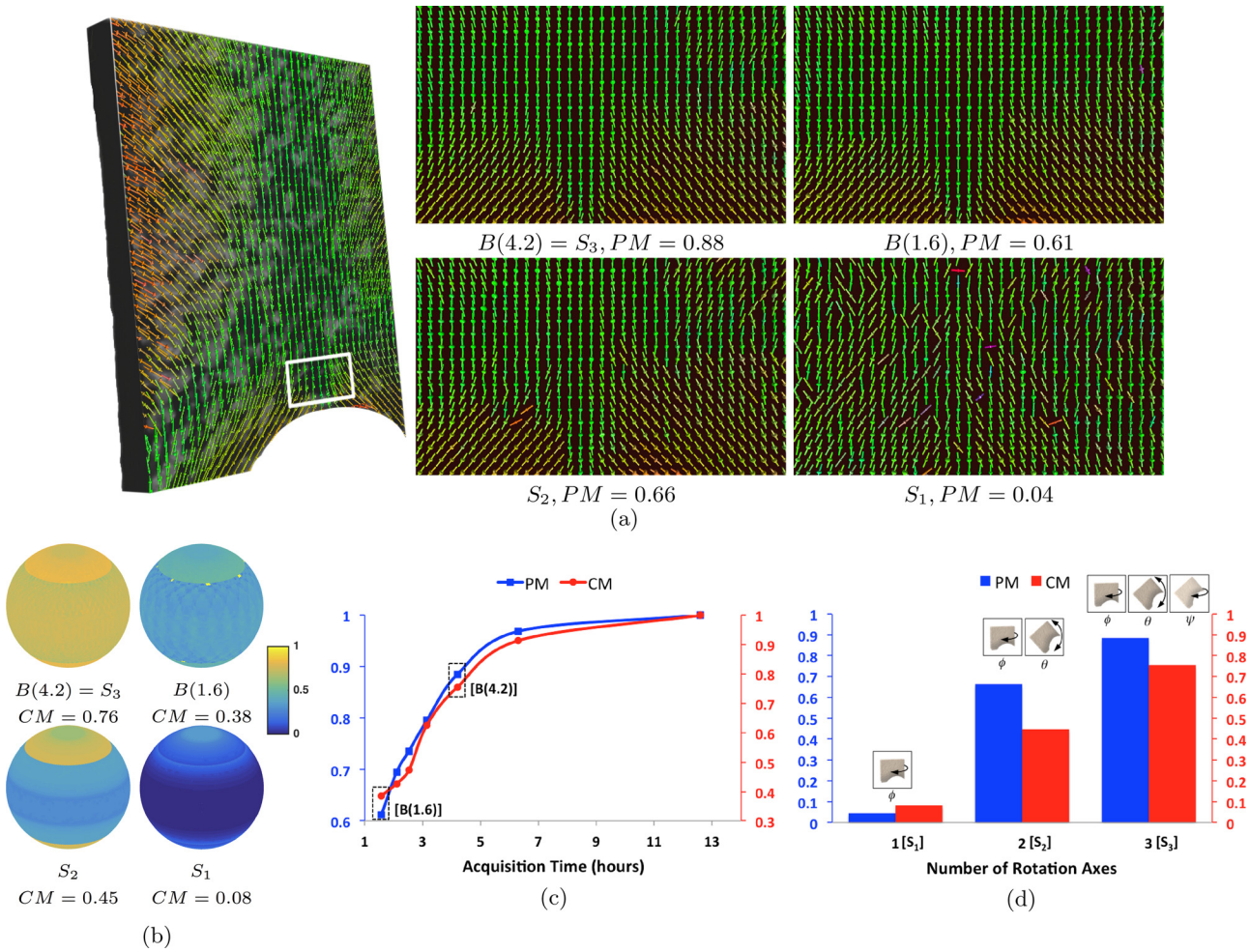

FIG. 4. Quantitative and qualitative comparison of four different acquisition protocols: $B(4.2)$ (also called S_3) employs 3 rotation axes and requires 4.2 h to measure; $B(1.6)$ employs 3 rotation axes and requires 1.6 h to measure; and S_2 requires only 2 rotation axes and 4.2 h measurement time while S_1 uses only 1 rotation axis with 1 hour acquisition time. (a) Reconstructed scattering tensors of the SFRP sample overlaid on the 3D image obtained using XCT (left); tensors in the region of interest for the four acquisition schemes (right). The visualizations are produced using CAMPVis.[19] (b) Corresponding Coverage Spheres for each scheme. (c) The effect of reducing the time of acquisition while employing all three rotation axes. (d) The effect of reducing the number of rotation axes.

$$PM(X) = \frac{|\{r_i;\, d(T_X(r_i), T_S(r_i)) < T_p,\ i = 1, \ldots, I\}|}{I},$$

where $T_p = 0.4$ and $|\cdot|$ is the number of elements in a set.

We now use the presented numerical (*CM*) and experimental (*PM*) approach for the relative quantification of acquisition schemes for two studies:

(a) *Effect of Acquisition Time*: Seven acquisition schemes $B(t)$ are defined by downsampling S to reduce the acquisition time to t hours while using all three axes of rotation

$$B(t) = \left\{ s_{(k-1)\times\frac{T}{t}};\quad k = 1, 2, \ldots, 2160 \times t/T \right\},$$

where $T = 12.6$ h is the acquisition time for scheme S. *CM* and *PM* for $B(t)$ are plotted against t in Figure 4(c). We pick two points $B(4.2)$ and $B(1.6)$ from Figure 4(c) and show the reconstructed result in the top row of Figure 4(a) and corresponding Coverage Spheres in the top row of Figure 4(b). It can be seen that $B(4.2)$ provides a uniform Coverage Sphere comprised of high values, thus leading to a good quality of the result.

(b) *Effect of Hardware Complexity*: Hardware complexity is induced by the Eulerian cradle, which is required to provide the two additional axes of rotation (ψ and θ). Therefore, in this study, we begin with the acquisition scheme $B(4.2)$ as representative of a complex setup employing 3 rotation axes and rename it S_3, the subscript here indicating the number of rotation axes. Next, we remove rotation axes in steps to obtain the schemes S_2 and S_1. Scheme S_2 represents a medium complexity setup employing two rotation axes with fixed ψ (optimally chosen using *CM*), while scheme S_1 represents a simple setup employing only one rotation axis (fixed ψ and θ)

$$S_2 = \{(\psi, \theta, \phi);\quad \psi = 40^\circ,\ \theta \in \Theta,\ \phi \in \Phi\},$$
$$S_1 = \{(\psi, \theta, \phi);\quad \psi = 40^\circ,\ \theta = 30^\circ,\ \phi \in \Phi\}.$$

The Coverage Spheres for S_2 and S_1 are shown in Figure 4(b), and the reconstructed tensors are shown in Figure 4(a). The plot of *CM* and *PM* versus the number of rotation axes is shown in Figure 4(d). It can be seen that the quality of the reconstruction deteriorates slightly but not enough to affect their interpretation in an application when only a single value

of ψ is used (i.e., a medium complexity setup using two rotation axes). However, using a simple setup with just one rotation axis and fixed ψ, θ (scheme S_1) markedly deteriorates the quality of the reconstructions. This indicates that a compact setup of medium complexity, employing only two rotation axes, can be sufficient for XTT. The *CM* calculation can be extended in future work to incorporate prior information about the sample and to determine the exact value(s) of θ required to measure all the structure orientations within the sample.

We conclude that it is possible to perform a full six-dimensional X-ray Tensor Tomography technique with at most two axes of sample rotation. Therefore, by adding only one additional rotation axis to a conventional X-ray Computed Tomography device, it is possible to obtain compact XTT setups for industrial and potential medical applications.

This work was funded by the European Commission under Grant Agreement No. 605162 (BERTI) and the DFG Cluster of Excellence, Munich-Centre for Advanced Photonics (MAP). The authors wish to thank Dr. Johann Kastner for providing the sample used in this study. Additional support was also provided by DFG Gottfried Wilhelm Leibniz program, the TUM Institute for Advanced Study and the Karlsruhe Nano Micro Facility (KNMF, www.kit.edu/knmf), a Helmholtz Research Infrastructure at Karlsruhe Institute of Technology (KIT).

[1]A. Momose, S. Kawamoto, I. Koyama, Y. Hamaishi, K. Takai, and Y. Suzuki, Jpn. J. Appl. Phys. **42**, L866 (2003).
[2]F. Pfeiffer, T. Weitkamp, O. Bunk, and C. David, Nat. Phys. **2**, 258 (2006).
[3]F. Pfeiffer, M. Bech, O. Bunk, P. Kraft, E. F. Eikenberry, C. Brönnimann, C. Grünzweig, and C. David, Nat. Mater. **7**, 134 (2008).
[4]W. Cong, F. Pfeiffer, M. Bech, and G. Wang, J. Opt. Soc. Am. A **29**, 908 (2012).
[5]G. Pelzer, A. Zang, G. Anton, F. Bayer, F. Horn, M. Kraus, J. Rieger, A. Ritter, J. Wandner, T. Weber, A. Fauler, M. Fiederle, W. S. Wong, M. Campbell, J. Meiser, P. Meyer, J. Mohr, and T. Michel, Opt. Express **22**, 24507 (2014).
[6]Z. Wang, N. Hauser, G. Singer, M. Trippel, R. A. Kubik-Huch, C. W. Schneider, and M. Stampanoni, Nat. Commun. **5**, 3797 (2014).
[7]F. Prade, A. Yaroshenko, J. Herzen, and F. Pfeiffer, Europhys. Lett. **112**, 68002 (2015).
[8]M. Strobl, Sci. Rep. **4**, 7243 (2014).
[9]F. L. Bayer, S. Hu, A. Maier, T. Weber, G. Anton, T. Michel, and C. P. Riess, Proc. Natl. Acad. Sci. **111**, 12699 (2014).
[10]F. Bayer, S. Zabler, C. Brendel, G. Pelzer, J. Rieger, A. Ritter, T. Weber, T. Michel, and G. Anton, Opt. Express **21**, 19922 (2013).
[11]W. Yashiro, S. Harasse, K. Kawabata, H. Kuwabara, T. Yamazaki, and A. Momose, Phys. Rev. B **84**, 094106 (2011).
[12]F. Schaff, A. Malecki, G. Potdevin, E. Eggl, P. B. Noël, T. Baum, E. G. Garcia, J. S. Bauer, and F. Pfeiffer, Sci. Rep. **4**, 3695 (2014).
[13]T. H. Jensen, M. Bech, O. Bunk, T. Donath, C. David, R. Feidenhans'l, and F. Pfeiffer, Phys. Med. Biol. **55**, 3317 (2010).
[14]A. Malecki, G. Potdevin, T. Biernath, E. Eggl, K. Willer, T. Lasser, J. Maisenbacher, J. Gibmeier, A. Wanner, and F. Pfeiffer, Europhys. Lett. **105**, 38002 (2014).
[15]J. Vogel, F. Schaff, A. Fehringer, C. Jud, M. Wieczorek, F. Pfeiffer, and T. Lasser, Opt. Express **23**, 15134 (2015).
[16]K. V. Mardia and P. E. Jupp, "Distributions on spheres," in *Directional Statistics* (John Wiley and Sons, Inc., 2008), pp. 159–192.
[17]D. Salaberger, K. A. Kannappan, J. Kastner, J. Reussner, and T. Auinger, Int. Polym. Process. **26**, 283 (2011).
[18]C. Hannesschläger, V. Revol, B. Plank, D. Salaberger, and J. Kastner, Case Stud. Nondestr. Test. Eval. **3**, 34 (2015).
[19]C. Schulte zu Berge, A. Grunau, H. Mahmud, and N. Navab, *CAMPVis—A Game Engine-inspired Research Framework for Medical Imaging and Visualization, Tech. Rep.* (Technische Universität München, 2014).
[20]X. Pennec, P. Fillard, and N. Ayache, Int. J. Comput. Vision **66**, 41 (2006).